
# A mean-field phase separation model enabling the coupling of non-isothermal flow phenomena with fibre formation in high-moisture

Journal of Food Engineering 412 (2026) 112972

Contents lists available at ScienceDirect

Journal of Food Engineering

journal homepage: www.elsevier.com/locate/jfoodeng

# A mean-field phase separation model enabling the coupling of non-isothermal flow phenomena with fibre formation in high-moisture extrusion of meat analogues

Erik Kaunisto [a], Camilla Öhgren [a], Niklas Lorén [a], Mats Stading [a,b,*]

[a] RISE – Research Institutes of Sweden AB, Department of Food Science and Innovation, Gothenburg, Sweden
[b] Chalmers University of Technology, Department of Industrial and Materials Science, Gothenburg, Sweden

ARTICLE INFO

*Keywords:*
Meat analogues
High moisture extrusion
Phase separation
Wall-slip
Simulation
Finite element model
Microscopy

ABSTRACT

In this study, a coupled model integrating flow, temperature, phase separation, fibre alignment, and wall-slip has been developed to elucidate the complex behaviour observed during high moisture extrusion (HME) fibre formation. By departing from previous high-resolution approaches, the model uses a mean-field simplification to conveniently address wall-slip, thus avoiding the numerical intractability associated with resolving microscopic phases through solving the full Cahn-Hilliard equations. The critical simulation parameters are justified through prior studies and microscopy data and may to a certain extent be quantifiable from dead-stop experiments. The model can capture key qualitative features of HME, including the spatial distribution of fibres in the cooling die and their orientation, as observed in microscopy. Moreover, the model explains a potential delicate interplay between die cooling, phase separation/syneresis and protein melt flow characteristics. The study identifies extensional and pre-cooling die orientation of fibres as promising avenues for future model refinement.

## 1. Introduction

Global meat consumption has doubled from 1961 to 2009 and is still on the rise (Steinfeld, 2006). The food sector is responsible for 25 % of all greenhouse gas emissions, with meat production alone accounting for a significant 14.5 % (Gerber et al., 2013). This surge in meat consumption is concerning from a nutritional standpoint as well, as excessive intake of especially red meat has been associated with health issues like coronary heart disease and certain types of cancer (Di et al., 2023; Glenn et al., 2024; Tammi et al., 2024). Plant-based alternatives to meat, meat-analogues, are for these and other reasons gaining popularity.

Fibrous meat-analogues are currently produced commercially from soy and pea protein, as well as from wheat gluten, using an extruder to create a protein melt under high moisture, temperature, and pressure, followed by active cooling upon exit. Similar fibre formation techniques are used in plastics production to enhance material strength (Ardakani et al., 2013). A common factor in fibre formation for both meat analogues and plastics is that the production process is known, but the mechanisms behind fibre formation are not fully understood. Existing hypotheses on the mechanisms provide insights but are insufficient for a complete explanation and cannot fully predict the fibre formation capability of protein melts. This limitation hinders the use of more sustainable protein sources in meat analogue production and limits the speed of processing. Hypotheses and models range from "chemical," highlighting the interactions between protein chains or polymer crystallites, to "physical," focusing on fluid dynamics, heat transfer, phase separation, melt fracture and deserve a more detailed presentation, as further elaborated upon below.

Structural effects of covalent and non-covalent bonds has been studied, but does not provide a concrete kinetic fibre formation mechanism (Chen et al., 2011). In another model, extensional, kinetic energy and Poisson's ratio-based mechanisms have been investigated for polytetrafluoroethylene (PTFE) and refer fibre formation to a consequence of forced attraction between polymer particles by extensional flow, thus neglecting the possible significance of shear contributions (Ardakani et al., 2013; Patil et al., 2006; Vavlekas et al., 2017). The model is highly relevant for the structure formation in PTFE, but as it describes fibre formation as reversible the relevance is limited for extrusion of high moisture meat analogues (HMMA).

Several groups have proposed models based on phase separation coupled with heat transfer and mechanical deformation (Kaunisto et al., 2024; Sandoval Murillo et al., 2019; van der Sman and van der Goot,

* Corresponding author. RISE – Research Institutes of Sweden AB, Department of Food Science and Innovation, Gothenburg, Sweden
*E-mail address:* mats.stading@ri.se (M. Stading).

https://doi.org/10.1016/j.jfoodeng.2026.112972
Received 20 August 2025; Received in revised form 5 January 2026; Accepted 7 January 2026
Available online 7 January 2026

2023; Wittek et al., 2021). The cooling die cools the melt from the outside causing high melt viscosity along the walls and effectively a funnel-shaped flow profile with high flow of hot melt in the centre of the die and slow flow of cold melt along the walls (Högg et al., 2017; Kaunisto et al., 2024; Osen and Schweiggert-Weisz, 2016; Sandoval Murillo et al., 2019). This causes extensional flow in the centre and high shear in the transition zone between cold and hot melt flow. Structure formation is assumed to arise from phase separation into a protein-rich and a protein-poor phase under a critical temperature, and can be described by the Cahn-Hilliard model (Cahn and Hilliard, 1958). The phase separation has been simulated under the assumption of spinodal decomposition (Kaunisto et al., 2024; Sandoval Murillo et al., 2019), and has alternatively been suggested to possibly depend on cross-linking (van der Sman and van der Goot, 2023). The Cahn-Hilliard model only postulates phase separation under a critical temperature, but an underlying multi-phase system has also been suggested to occur already in the hot screw section of the extruder, based on dead-stop experiments (Wittek et al., 2021). The fibrous structure induced by the phase separation was simulated and fibres were found to align in the high-shear flow regions of the cooling die (Kaunisto et al., 2024; Sandoval Murillo et al., 2019). The shear structuring has been thoroughly studied by the Van der Goot group, but in a shear-cell rather than in an extruder cooling die (Cornet et al., 2022; Dekkers et al., 2018; Grabowska et al., 2014).

The fibrous structure in HMMA has also been suggested to arise from viscoelastic mass fracture arising from flow instabilities such as melt-fracture trapped by distinct solidification (Guan et al., 2024; Sägesser et al., 2025). A sudden drop in shear viscosity was observed when shearing soy-protein and pea protein melts in a high pressure cell (Sägesser et al., 2025).

High moisture extrusion (HME) of HMMA has two main experimental challenges in validating any of the suggestions and models: harsh conditions in the extruder and the unstable nature of the extrudates. Extrusion is typically performed at temperatures up to 150 °C and high pressure like 10 bars, which is difficult to reproduce in any experimental technique. Furthermore, any experimental method that should mimic extruder conditions must involve significant deformation, as that drives structure formation. The extrudates in themselves also pose a challenge. Pulled pork can be used as a metaphor in explaining the dilemma. It appears solid and structureless until deformed, and when pulled apart the fibres appear. The extrudates appear solid and fibres appear only when the extrudates are deformed, frozen-thawed or swelled (Lorén et al., 2025; Nieuwland et al., 2023). Meso-scale areas formed by phase separation or other mechanisms have only been visualised after freezing or sample preparation (Lorén et al., 2025).

Experiments for validating models should preferably be performed directly in the extruder and the cooling die and there are a few reported results. A small extruder and cooling die was placed in a neutron beamline to elucidate nano-scale structure development during extrusion (Guan et al., 2024). Globular proteins (~9 nm) and nanoaggregates (~40 nm) were found throughout the cooling die and no further structuring at the nanoscale was observed. Flow profiles have been obtained directly in the cooling die using pulsed ultrasound velocity profiling (Kaunisto et al., 2025). Velocity profiles were accurately reproduced but the resolution close to the die wall was not sufficient to validate the bell-shaped velocity profiles predicted by simulation (Kaunisto et al., 2024). A popular experimental technique is “dead-stop” experiments, with or without added dyeing of the material, where the extruder is suddenly stopped, opened and samples collected along the extruder screws and in the cooling die (Chen et al., 2011; Högg et al., 2025; Wittek et al., 2021; Zhang et al., 2022). It gives information along the whole extrusion process such as arrested flow profiles and chemical composition, but as the method suddenly release the high pressure and drops the temperature it may change structures in the melt. The process also takes several minutes so the non-equilibrium state in the extruder will have time to relax.

In the present study we have added the effect of wall-slip on fibre formation to previously described mechanisms by using a practical and computationally faster mean-field simplification to avoid the numerical and theoretical difficulties associated with solving the Cahn Hilliard equations under wall-slip. The present study aims to couple wall-slip to phase separation mechanism, to explain an interplay between die cooling, phase separation/syneresis and protein melt flow characteristics.

## 2. Materials and methods

### 2.1. Experimental input data

The present study uses the same experimental input data and assumptions for pea protein from rheological measurements and literature, as we have previously presented (Kaunisto et al., 2024). The obtained power-law exponent for the protein melt at 62 % moisture content was $n = 0.13$ and the temperature dependence followed an Arrhenius-type expression, given in equation (1) below for convenience,

$$K(T) = z_1 * e^{\frac{z_2}{z_3 + T}} \tag{1}$$

where $z_1 = 100.2$, $z_2 = 637.9$ and $z_3 = 28.4$ with $T$ in degrees Celsius. The physical properties of the protein melt were $C_p = 3.39 \frac{kJ}{[KgK]}$, $k = 0.43 \frac{W}{[mK]}$ and $\rho = 1000 \left[\frac{kg}{m^3}\right]$, as defined in Section 3.2, giving a thermal diffusion coefficient $\alpha = \frac{k}{\rho C_p} \approx 0.127 \frac{mm^2}{s}$. The reader is referred to the previous study for more experimental details (Kaunisto et al., 2024).

### 2.2. Microscopy of extrudate samples

#### 2.2.1. Light microscopy

Microscopy data was obtained for extrudates at similar extrusion operating conditions, as mentioned in our previous study (Kaunisto et al., 2024) to enable a qualitative comparison with the simulations. A light microscope (LM, Olympus BX53F2) equipped with a CMOS colour camera (Olympus SC50) and the software Olympus CellSense Entry was utilized to visualise the extruded samples at different positions in the samples and from different directions. The samples were analysed using 4x, 10x, 20x, 40x and 100x objectives. The samples were prepared as follows: The extrudates were cut into pieces of approximately 1 × 2 × 4 mm in two different directions related to the extrusion direction. The rectangular blocks were airfixed by lying on a grid above formalin and glutaraldehyde in $CaO_3$ for 3 days in a closed chamber. The third day they were placed above 2 % $OsO_4$ for 3 h. In a graded series of ethanol solutions (50, 70, 90 and 100 % by volume) the samples were dehydrated at room temperature and subsequently embedded in epoxy resin (Technovit 7100). Sections of 1.0 μm were cut with an RMC Power Tome XL using glass knives; the samples were subsequently placed on glass slides. The sections were stained with Lugol's iodine solution to visualise the starch phase and the dye Light Green in acetic acid was used to visualise the protein phase.

#### 2.2.2. Confocal laser scanning microscopy

The extrudates were stained with 0.01 % Texas Red solution and Direct Yellow 96. Micrographs were acquired using confocal laser microscopy (CLSM; Leica TCS SP5, Heidelberg, Germany). A 488 nm argon laser and a 594 nm HeNe laser and an HCX PL APO CS 10.0×0.40 DRY UV objective, was used. Emissions were collected at 500–540 and 610–650 nm using an image format 1024 × 1024 pixels with an eight lines average.

## 3. Calculation and theory

### 3.1. Model and geometry assumptions

The present work uses similar model assumptions as we have previously presented (Kaunisto et al., 2024), where the fibre formation process can be effectively regarded as a phase separation process, although possibly connected to the hypothesized syneresis and solidification mechanisms in the cooling die (van der Sman and van der Goot, 2023). Further, the 2D parallel plate assumption is used (Kaunisto et al., 2024), where the half-width and length are set as 2.5 mm and 200 mm, respectively, in accordance with one modular section of the updated cooling die studied here.

### 3.2. Mathematical model

#### 3.2.1. Flow and temperature

The flow field is modelled as previously (Kaunisto et al., 2024) and stated here again for convenience. The stationary incompressible Navier-Stokes (NS) equations (2) and (3) are coupled to a calibrated temperature-dependent constitutive power-law model (4–5) and the associated stationary temperature field (6),

$$\rho \boldsymbol{u}\cdot\nabla\boldsymbol{u} = -\nabla p + \nabla\cdot\left[\mu_{eff}\left(\nabla\boldsymbol{u} + (\nabla\boldsymbol{u})^{T}\right)\right] \tag{2}$$

$$\nabla\cdot\boldsymbol{u} = 0 \tag{3}$$

$$\mu_{eff} = K(T)\dot{\gamma}^{n-1} \tag{4}$$

$$\dot{\gamma} = \sqrt{2u_x^2 + \left(v_x + u_y\right)^2 + 2v_y^2} \tag{5}$$

$$\rho C_p \boldsymbol{u}\cdot\nabla T = \nabla\cdot(k\nabla T) \tag{6}$$

where $\rho$ is the mass density, $\boldsymbol{u} = (u, v)$ is the flow field, $p$ is the pressure, $\mu_{eff}$ is the effective viscosity, $K$ is the consistency index, $n$ the power-law exponent, $T$ the temperature, $\dot{\gamma}$ the strain-rate scalar, $C_p$ is the specific heat capacity and $k$ the thermal conductivity. It can be noted that the definition of the strain-rate scalar in equation (5) follows that of Slattery (1999), corresponding to the strain rate in viscometric flows. Further, in the constitutive model, the temperature dependency is assumed to be carried solely by the consistency index parameter, similar to other work (Wittek et al., 2021). The main reason for working with a power-law constitutive model is, to the best of our knowledge, a lack of evidence in the literature for the significance of elongational effects in HMMA fibre formation. Another important reason is that such models are often hard to calibrate from available experimental data and may exhibit limited shear-thinning behaviour, as compared to the experimentally observed $n = 0.1 - 0.2$.

#### 3.2.2. Simplified phase separation model

As an alternative to using a thermodynamic potential when solving the Cahn-Hilliard equations for a random instantiation of the phase separated state in the extruder die (Kaunisto et al., 2024), the same thermodynamic potential was instead used as the basis to develop a simplified phase separation model to account for fibre formation. The thermodynamic potential is stated in equation (7) below for convenience.

$$\Psi = 2T_c Rc(1-c) + TR[(1-c)ln(1-c) + cln(c)] \tag{7}$$

where $c = \frac{\phi+1}{2}$ is the concentration, $\phi$ is the order parameter, $\Psi$ the symmetric thermodynamic potential, $T_c$ the critical temperature, $T$ is the temperature and $R$ the gas constant. The local equilibrium phase separation, $\beta_{eq} = |\phi_0|$, was calculated numerically by setting $\frac{\partial\Psi}{\partial\phi} = 0$, and solving for the order parameter, $\pm\phi_0$, for specific values of $T$ and $T_c$. An explicit expression, equation (8), was then fitted over the relevant potential temperature ranges, see Fig. 1,

$$\beta_{eq}(T_c, T) = \begin{cases} \left(p_1 T_c^2 + p_2 T_c + p_3\right) tanh\left[\left(p_4 T_c^2 + p_5 T_c + p_6\right)(T_c\text{-}T)\right]^{(p_7 T_c + p_8)}, & for\ T < T_c \\ 0, & for\ T \geq T_c \end{cases} \tag{8}$$

where $p_1 = -4.33\times10^{-5}$, $p_2 = 1.16\times10^{-2}$, $p_3 = 1.94\times10^{-1}$, $p_4 = 1.50\times10^{-6}$, $p_5 = -4.00\times10^{-4}$, $p_6 = 3.40\times10^{-2}$, $p_7 = -1.48\times10^{-4}$ and $p_8 = 5.07\times10^{-1}$ are the fitted parameters, as determined by non-linear regression. The use of a hyperbolic tangent construction is a natural choice due to the inherent symmetry, smoothness and sigmoid-like behaviour of the phase transition, as governed by the thermodynamic potential. Fig. 1 shows that equation (8) accurately captures the equilibrium order parameter to be conveniently used in a simplified phase separation model for any given and valid $T_c$. Thus, a stationary mean-field transport equation for the local amount of phase separation can be formulated according to equation (9)

$$-\nabla\cdot\left[\frac{0.1D(T_c)K(T_c)}{K(T)}\nabla\beta\right] + \boldsymbol{u}\cdot\nabla\beta = \frac{D(T_c)}{\varepsilon^2}\frac{K(T_c)}{K(T)}\left(\beta_{eq}(T_c, T) - \beta\right) \tag{9}$$

where $\beta$ is the local amount of phase separation, defined on the interval [0,1], $\varepsilon$ is the characteristic distance between phase separated domains and $D(T_c) = 0.1\alpha$ is the diffusion coefficient with an associated scaling with the consistency index, as previously discussed by Kaunisto et al., (2024); Sandoval Murillo et al., 2019; Kaunisto et al. (2024). Equation (9) accounts for the local average production and convection of phase separated fluid material with a relatively small added diffusion term for numerical smoothing. It should be noted here that the characteristic distance between phase separated domains needs to be small enough for

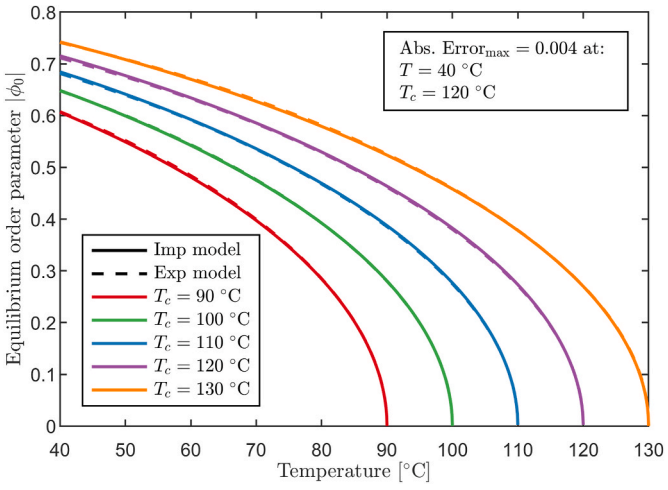


**Fig. 1.** Comparison between the fitted explicit expression and implicit solutions for the equilibrium order parameter as a function of temperature.

the present coarse-grained model to be arguably valid and that interfacial surface tension and gradient penalization effects are not explicitly modelled.

An inherent challenge with using a scalar field to represent fibre formation is the lack of orientational information regarding fibre alignment, which is crucial for the texture of HMMAs. Recent literature suggests that fibres are likely the result of multiscale texturization mechanisms (van der Sman and van der Goot, 2023), including non-isothermal shear flow, making it arguably non-trivial to define a meaningful fibre orientation through a conformation tensor approach, such as the Folgar-Tucker model (Folgar and Tucker, 1984). However, it seems reasonable that the local accumulated shear in the cooling die could act as an approximation of the amount of multiscale fibre alignment that can be expected. Therefore, an additional simple transport equation (10) is proposed,

$$-\nabla\cdot\left[\frac{0.1D(T_c)K(T_c)}{K(T)}\nabla\theta\right]+\boldsymbol{u}\cdot\nabla\theta=\frac{\dot{\gamma}(1-\theta)}{\theta_{res}} \tag{10}$$

where $\theta$ is the fibre alignment measure defined on the interval [0,1], and $\theta_{res}$ is the fluid resistance to alignment. Equation (10) assumes that alignment is produced by the local effective shear, i.e. the shear rate for viscometric flows. With both $\beta$ and $\theta$ defined, it is possible to define the oriented and randomly oriented fibre composite measures of the fluid as $F_o=\beta\theta$ and $F_{ro}=\beta(1-\theta)$, respectively, i.e. combining the effects of shear-induced fibre alignment and preservation of the structure through phase separation-induced solidification.

#### 3.2.3. Boundary conditions

The non-trivial boundary conditions in the present model are summarised in Fig. 2, showing the solution domain, $\Omega$, and associated boundaries, $d\Omega_i$ for $i=1,2,3,4,5$. Dirichlet conditions are used to specify assumed fully developed flow, $\boldsymbol{u}_{inlet}$, the inlet temperature, $T_{inlet}=140\,^{\circ}C$, phase separation, $\beta_{inlet}=0$ and alignment, $\theta_{inlet}=0$, at the inlet boundary $d\Omega_1$. A no-slip condition is used over the initial part of the cooling die, $d\Omega_2$, followed by a phase separation dependent wall-slip and a Dirichlet condition for the cooling temperature that are imposed on the remainder of the die length, $d\Omega_3$. The expression for the slip length, $L$, is based on a smooth ramping function, where a finite asymptotic slip length, $L_0=20\,mm$, and a regularization parameter, $\kappa=1\,mm$, are assumed to model the slip behaviour and to avoid numerical problems for low values of $\beta$. The physical justification for the current wall-slip condition is the hypothesized syneresis/solidification mechanism that expels water at the surface, thus creating a slippery surface. A symmetry condition is further imposed at the half-channel width, $d\Omega_4$, and at the die exit, $d\Omega_5$, a zero-pressure regular outlet condition is specified. In all other cases, and if not specified in Fig. 2, a natural boundary condition is used.

#### 3.2.4. Numerical implementation

The model is cast on weak form and implemented in COMSOL Multiphysics 6.3 (COMSOL, 2021), using a combination of existing fluid and heat flow interfaces and two custom PDE interfaces for a straightforward implementation of the simplified phase separation and alignment equations. Before solving, the necessary fitting parameters in equation (8) were generated with a simple MATLAB script and the smooth ramping function for the slip-condition was defined in COMSOL in terms of its dimensionless position and transition length arguments, 0.5 and 1, respectively , yielding values over the interval [0, 1] for a given $\beta$. The stationary model was then solved by using the PARDISO stationary parametric solver, where the wall temperature was ramped down from the inlet temperature to the specified wall cooling temperature. The initial guess for the solution variables was a fully developed velocity profile, $\boldsymbol{u}=\boldsymbol{u}_{inlet}$, $T=T_{inlet}$, $\beta=\beta_{inlet}$ and $\theta=\theta_{inlet}$. A mesh density of approximately 140,000 triangular mesh elements over the given solution domain (see section 3.1 and Fig. 2) was used to solve all the equations. The equation system was quite stiff with a solution time in the order of days on an Intel® Xeon® w5-3435X, 3096 MHz, 16 Core(s), 32 Logical Processor(s) with 256 GB RAM, depending on parameter settings. Mesh convergence was also checked for the flow variables to ensure a converged solution.

## 4. Results

### 4.1. Impact of cooling temperature

#### 4.1.1. Additional simulation parameters

The model was used to study the impact of cooling temperature on the flow profiles in the extruder die and specifically at the extruder die outlet. A maximum inlet velocity of 5 mm/s and critical temperature for phase separation, $T_c=110\,^{\circ}C$, was specified in accordance with previous studies (Kaunisto et al., 2024; Sandoval Murillo et al., 2019). In addition, a characteristic distance between phase separated domains, $\varepsilon=50\,\mu m$, and a fluid resistance to alignment, $\theta_{res}=100$. The values of the latter two parameters are further discussed in relation to Section 4.3 and Section 5.

#### 4.1.2. Extruder die flow profile

The effect of varying cooling temperature on the velocity profile in the extruder die is shown in Fig. 3. Fig. 3A shows small initial deviations from the fully developed inlet flow profile already at a cooling temperature corresponding to the critical temperature of 110 °C, where the flow exhibits a weak initial core slip caused by the formation of a viscosity-induced funnel, as earlier pointed out (Kaunisto et al., 2024), where recovery of the inlet flow profile is then achieved towards the end of the die due to limited cooling. On the other hand, in Fig. 3B, the initial core slip is stronger by the lowered cooling temperature, resulting in both relatively higher thermal penetration and phase separation that, in

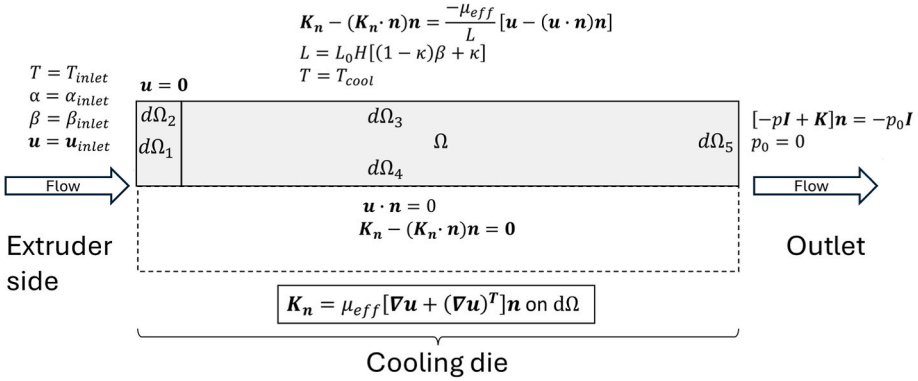


**Fig. 2.** Schematic picture of the simulated die geometry with the non-trivial boundary conditions.

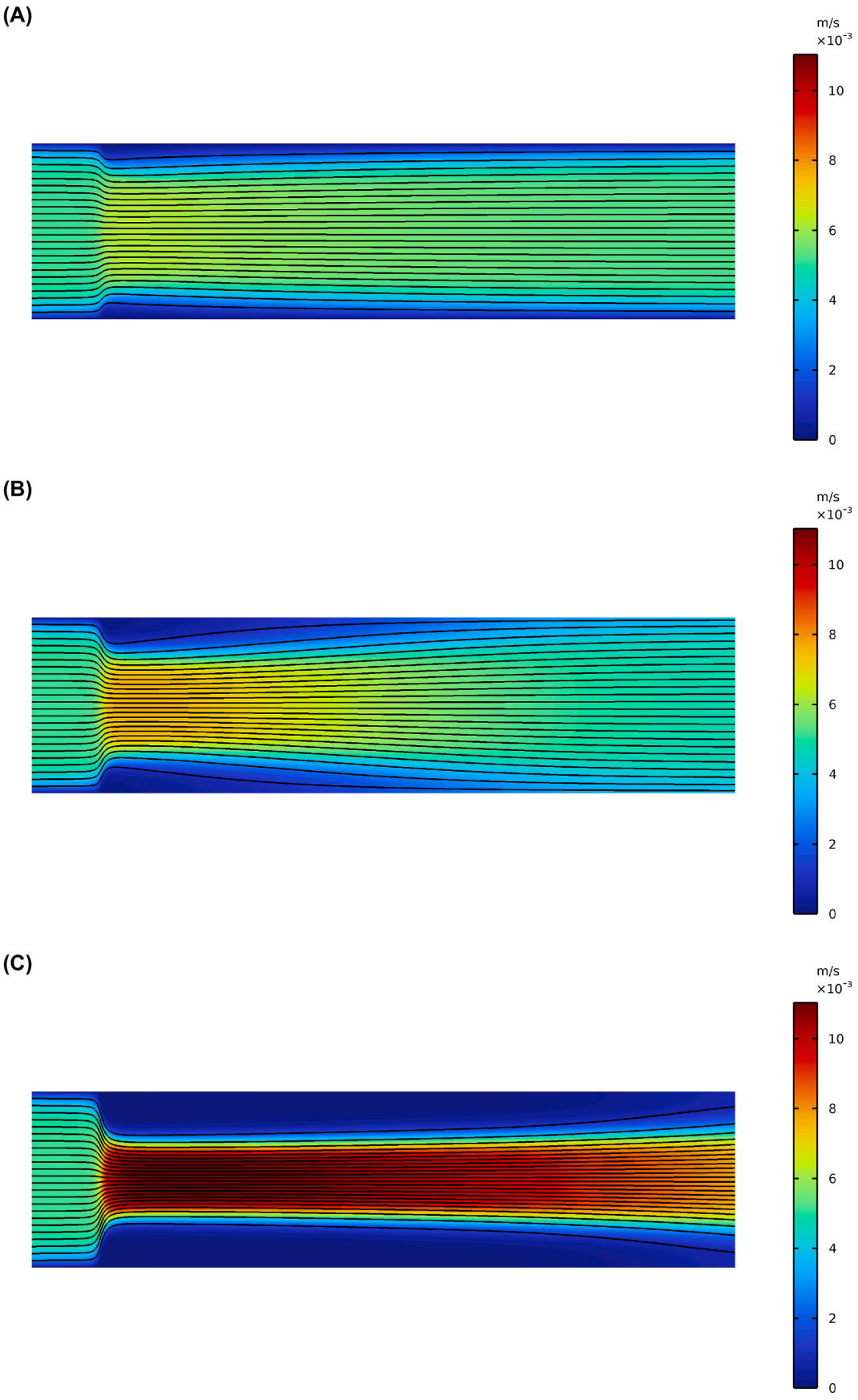


**Fig. 3.** Velocity magnitude, $|\boldsymbol{u}|$, and streamlines (black) in the cooling die at three different cooling temperatures for (A) $T_{cool} = 110\,^{\circ}C$, (B) $T_{cool} = 90\,^{\circ}C$ and (C) $T_{cool} = 60\,^{\circ}C$.

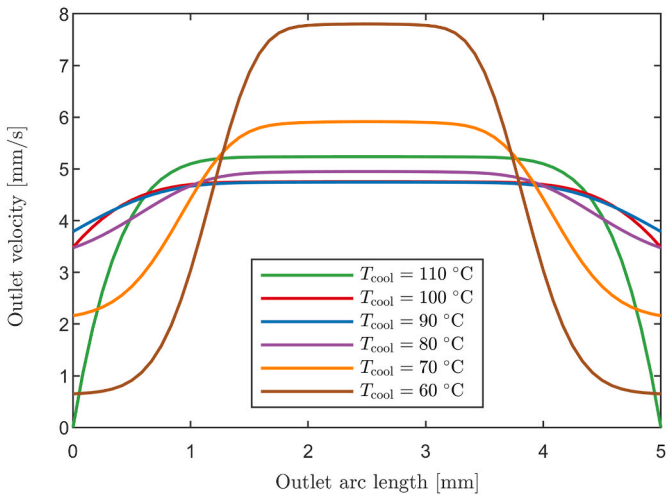


**Fig. 4.** Outlet cross-sectional velocity profile, $|\boldsymbol{u}|$, for different cooling temperatures.

turn, causes wall-slip and a transition towards plug flow. In contrast to Fig. 3A, continuity and loss of wall-shear require the peripheral streamlines to bend significantly from the high-shear initial core-slip region of Fig. 3B towards the sides of the die, whereas the central streamlines remain essentially unaffected. When the fluid is further cooled, the initial core-slip and central velocity are too strong, implying that thermal penetration, phase separation and wall-slip cannot manage to recover the plug flow over the remainder of the die, as shown in Fig. 3C.

#### 4.1.3. Die outlet velocity profile

The shape of the velocity profile at the outlet was investigated for different cooling temperatures, as illustrated in Fig. 4. For higher cooling temperatures, the velocity profile shows a regular shear-thinning velocity profile with higher velocity gradients at the wall due to the low wall-slip. However, close to a cooling temperature of 90 °C, the flow reaches almost plug flow like behaviour and then switches to an s-shape, with stronger core-slip, at even lower cooling temperatures. The results in Figs. 3–4 thus provide a potential explanation for the delicate interplay between protein melt rheology, wall-slip, thermal penetration and phase separation to yield optimal conditions for fibre formation during high moisture extrusion.

### 4.2. Fibre formation

#### 4.2.1. Local amount of phase separation

To further explain the onset of wall-slip, the local amount of phase separation in the extruder die was assessed. In Fig. 5A–C, phase separation is plotted against three different cooling temperatures, illustrating the varying degree of solidification and thermal penetration. In Fig. 5A, the subcooling below the critical temperature is too low, causing limited phase separation towards mainly the edges of the die and a weak wall-slip. In Fig. 5B, the flow situation is that of Fig. 3B where wall-slip increases, yielding longer residence times towards the end of the die, improved thermal penetration and phase separation. With further subcooling in Fig. 5C with the corresponding flow situation in Fig. 3C, the thermal penetration is indeed further increased, causing more phase separation at the edges and in the core towards the end of the die, but the resulting core-slip and lack of plug flow would make the associated operating conditions unfeasible in this case.

#### 4.2.2. Fibre alignment measure

To investigate how the fluid is subjected to shear-induced fibre alignment, the associated measure was plotted for the same temperatures as in Fig. 5, see Fig. 6. Alignment is being produced already at walls in the fully developed inlet region in Fig. 6A–C with a broadening of the production region towards the centre of the cooling die. In Fig. 6B the alignment seems to be gradually produced in the cooled fluid region closer to the walls, either due to the longer residence times or the higher shear in the transition towards the inner core. When the plug flow is formed due to increasing slip, the alignment is further advected along the streamlines to the walls, for reasons of continuity, thus contributing to a potential gradual concentration of alignment in this region and along the length of the cooling die. In Fig. 6C the alignment is even more pronounced towards the centre of the cooling die, although not feasible, as previously mentioned.

#### 4.2.3. Composite fibre measure

The local amount of phase separation and resistance to fluid alignment were used to assess the composite measures of fibre formation, see Fig. 7. From Fig. 7A and B it is evident that the present model predicts oriented fibres close to the walls and randomly oriented fibres in the core. These results are consistent with our previous simulation results (Kaunisto et al., 2024), although with the added refinement of accounting for the non-trivial effects of wall-slip. Notably though, the oriented fibres are quickly and continuously formed along the cooling die, whereas the die length and transition to plug flow both contribute to the increased thermal penetration and formation of the randomly oriented fibres.

### 4.3. Light microscopy and model validation

To validate the model, extrudates have been studied visually on the micrometre scale, see Fig. 8A, where a planar image of the extrudate with a perspective as in the simulations has been generated by cutting from the side and about 1 cm into the sample. Fig. 8B–D shows how the structure looks near either the bottom or the top edge of the extrudate, while Fig. 8E shows the structure in the middle. As can be seen in Fig. 8A, the extrusion direction (from left to right) in the sample is visible and protein fibre strands are delimited by areas that contain either a lower proportion of protein or bran components or starch. At an overall level of structure in the CLSM image in Fig. 8B and in the LM image in Fig. 8C, with slightly higher magnification, the protein is seen to form fibres with an average width of about 40–80 μm, which corresponds well with a characteristic distance between phase separated domains of 50 μm. The LM image in Fig. 8D shows the oriented protein phase close to the top or bottom edges at high magnification, while the LM-image in Fig. 8E shows a more randomly distributed protein phase, which is obtained from the middle of the extrudate, at the same magnification. The fact that different degrees of fibre orientation are obtained at different positions is in good agreement with the simulation model.

## 5. Discussion

The present study aims to couple flow, temperature, phase separation, fibre alignment and wall-slip to explain observed flow and fibre formation characteristics during HME extrusion, where the model simplifications, as compared to previous work, deserve to be discussed. In this regard, it is important to emphasize that solving e.g. the full Cahn-Hilliard equations for a time-dependent random instantiation of the phase separated state is of practical limited value when formulating a simplified wall-slip condition. That is, if the microscopic details of the phases are resolved by an alternative model, and thus allowed to randomly alternate at the wall, both viscosity and the wall condition should vary significantly over very small length scales. The latter would make the model numerically intractable, and the present mean-field approach therefore seems to be a reasonable compromise to account for wall-slip. However, if phase separation is considered fast, one could consider just solving equation (8) algebraically for the equilibrium value

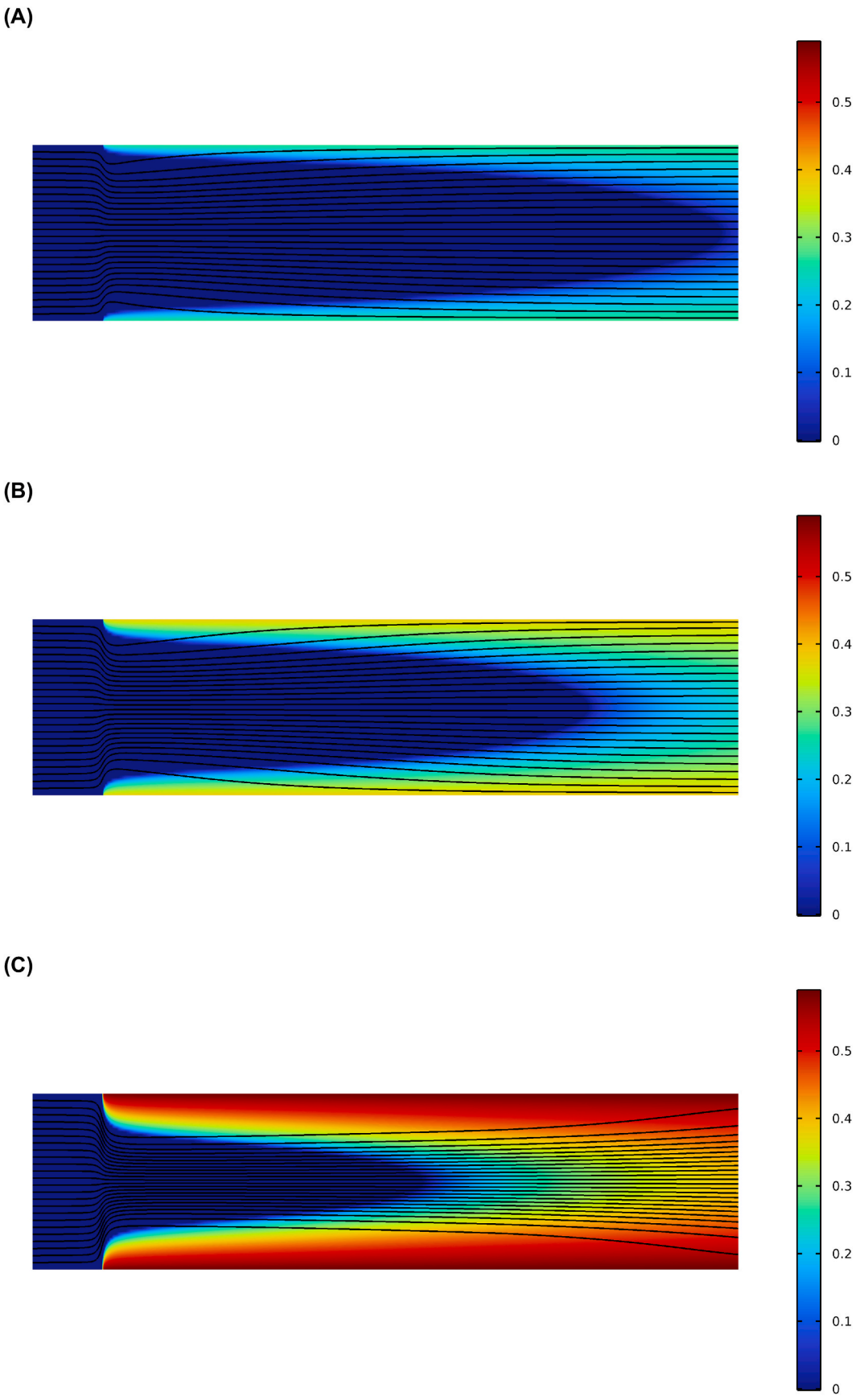


**Fig. 5.** Local amount of phase separation, $\beta$, and streamlines (black) in the cooling die at three different cooling temperatures for (A) $T_{cool} = 100\ ^{\circ}C$, (B) $T_{cool} = 90\ ^{\circ}C$ and (C) $T_{cool} = 60\ ^{\circ}C$.

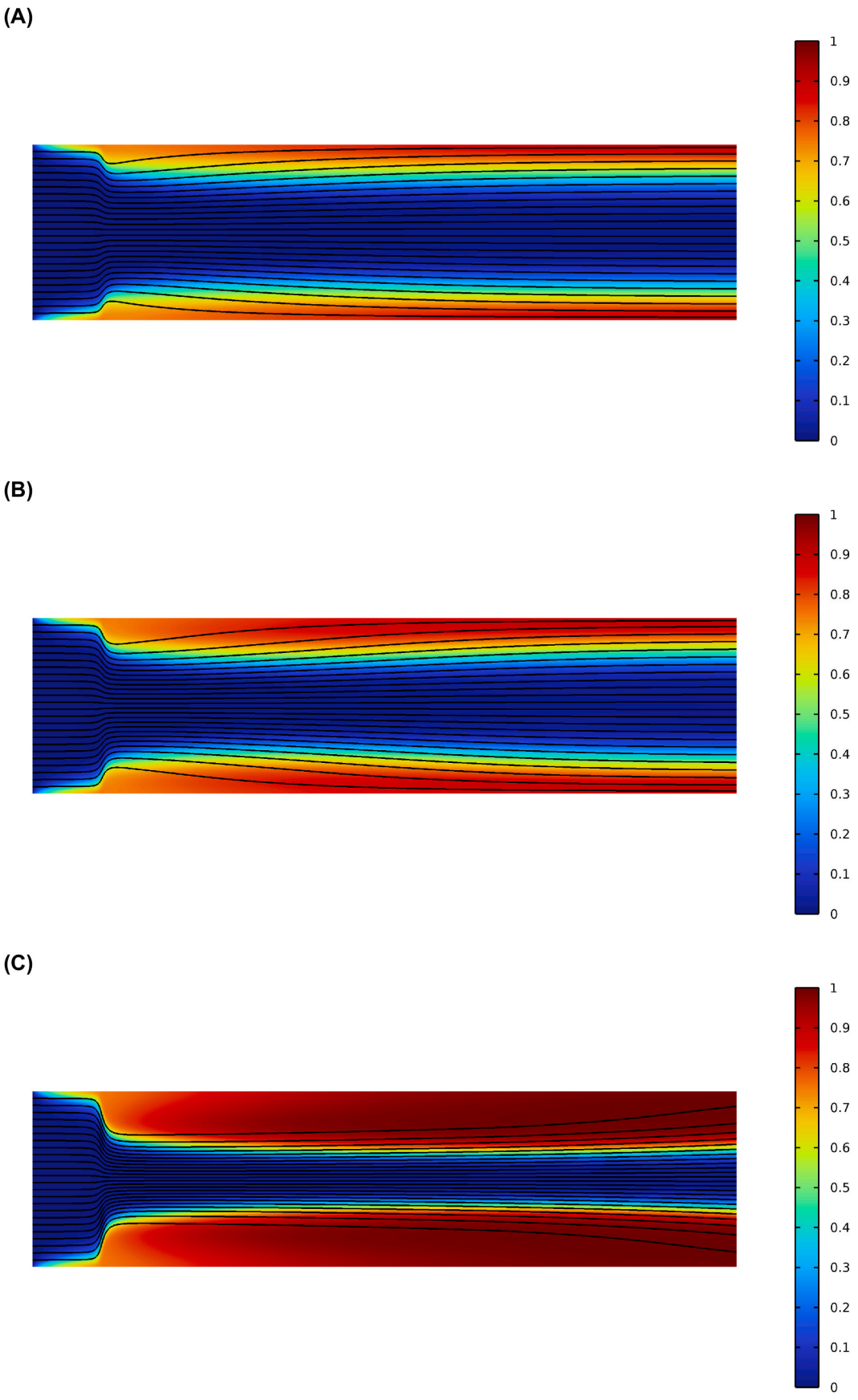


**Fig. 6.** Fibre alignment measure, $\theta$, in the cooling die and streamlines (black) for three different cooling temperatures for (A) $T_{cool} = 100\,^{\circ}C$, (B) $T_{cool} = 90\,^{\circ}C$ and (C) $T_{cool} = 60\,^{\circ}C$.

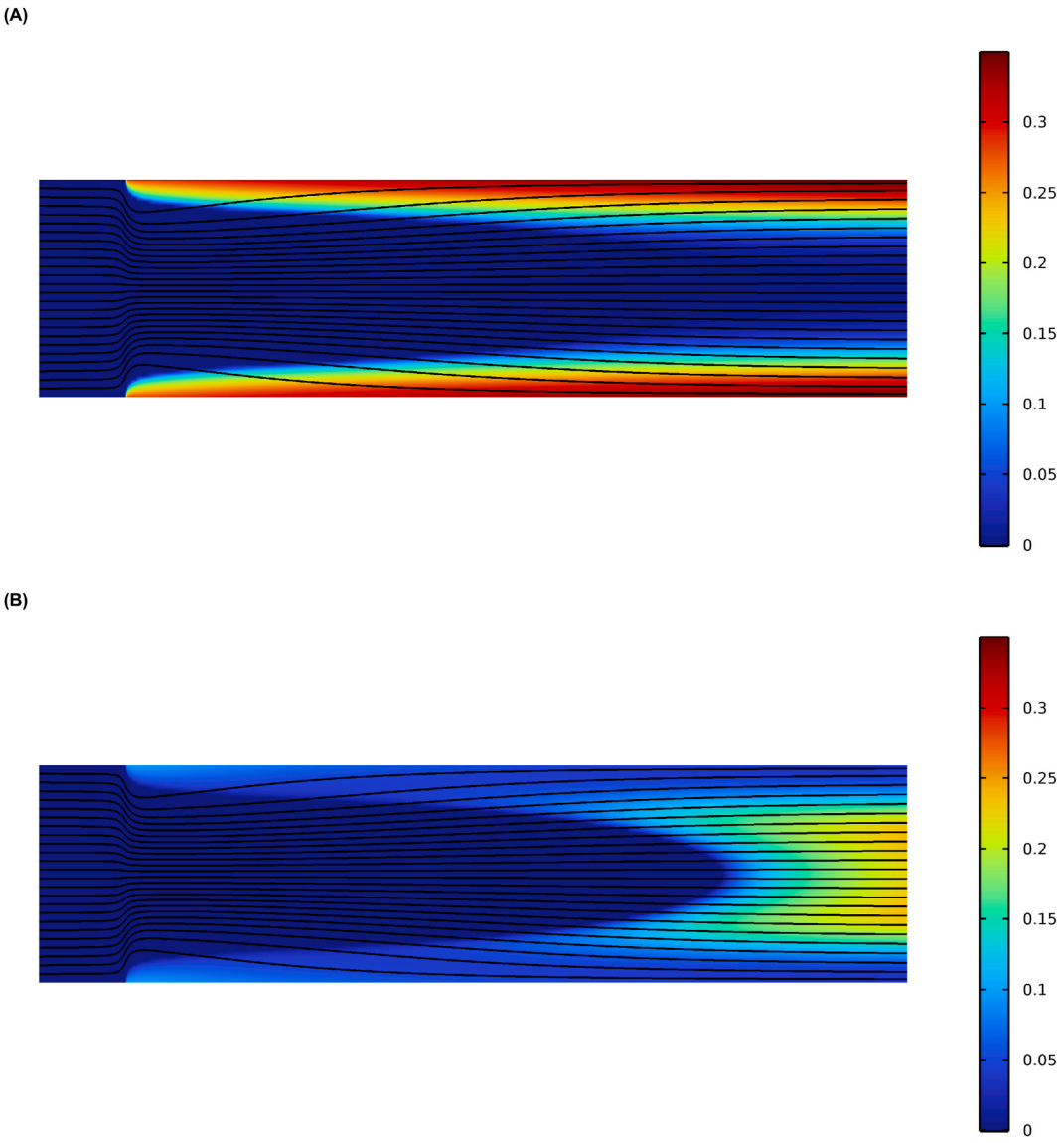


**Fig. 7.** Composite fibre measures at $T_{cool} = 90\,^{\circ}C$ in the cooling die and streamlines (black) for (A) oriented fibres, $F_o$, and (B) randomly oriented fibres, $F_{ro}$.

to reduce the numerical complexity of the model, and for direct use in the boundary condition for the wall-slip. Such an approach would imply that the temperature would act as the natural proxy variable for phase separation, which would disregard any significant resistances to mass transfer at the boundary.

Regarding the temperature boundary condition, it should also be mentioned that a cooling temperature of 100–110 °C naturally requires pressurized water or another medium. This is considered a detail, as the model parameters likely need to be calibrated so that the model predicts the same behaviour over other temperature ranges, as observed in any experiment. From previous studies and measurements, we have tried to justify the chosen simulation parameters, except for the fluid resistance to alignment. In principle, resistance to alignment could potentially be quantifiable to some degree from a dead-stop experiment, since unintentional fast solidification of the structure from flash cooling should preserve alignment, in contrast to the amount of phase separation. Nonetheless, the parameters chosen in this study are deemed sufficient to indicate the potential non-linear phenomena of fibre formation to be expected during HME. Importantly, from the light microscopy images of the extrudate cross-section, it can be concluded that the characteristic distance in the present study seems feasible. Moreover, the present study manages to qualitatively explain the observed distinction of oriented fibre and randomly oriented fibre domains close to the die wall and in the centre, respectively, where the creation and transport of alignment seems to play an important role.

As an alternative to the present model, one could assume that fibre formation and wall-slip is only dependent on e.g. temperature, local shear, critical shear stress and a fibre conformation tensor. Such an approach would however still raise questions on how to explain any potential coupling to the recently postulated syneresis or phase separation mechanism behind solidification, which is indeed addressed by the present model. On the other hand, it is worth noting that if shear history is considered the only mechanism behind fibre alignment, as in the present model, it is indeed hard to justify why HME processing would yield any oriented fibres in the centre of the cooling die. Additional mechanisms, e.g. extensional flow forming fibres in the core region of the die or pre-oriented fibres from the barrel section may thus be of complementary value to the present model. Future work may thus try to address any such discrepancies through further model development.

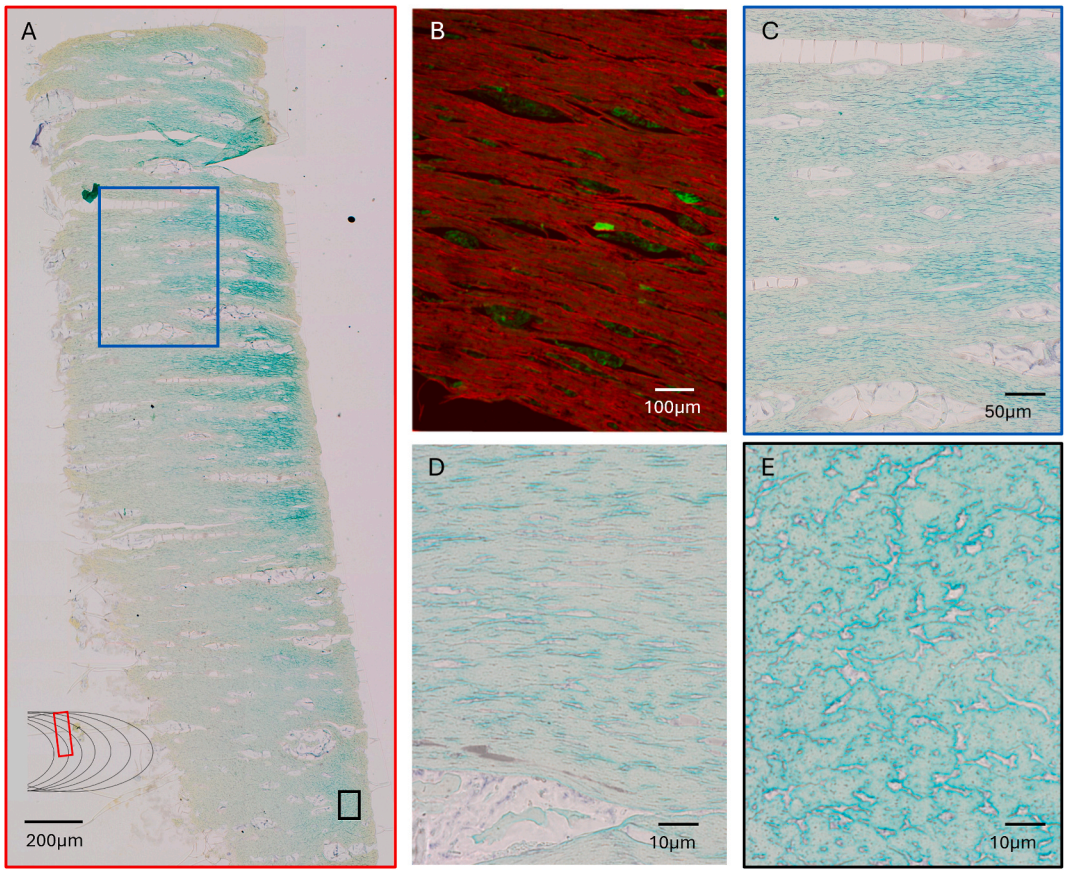


**Fig. 8.** (A) LM image of the extrudate sample like in the simulations at lower magnification and at a position as indicated by the red frames, (B) CLSM image and (C–E) LM images of an extrudate at different magnifications and positions with (B–D) close to the edges and (E) in the centre. The positions of (C) and (E) in (A) are indicated by the blue and black frames, respectively. The scale bars are (A) 200 μm, (B) 100 μm, (C) 50 μm and (D–E) 10 μm. Protein is shown in red in the CLSM image and in green in the LM images and fibres are green in the CLSM image and white in the LM image, where also starch is shown in violet. (For interpretation of the references to colour in this figure legend, the reader is referred to the Web version of this article.)

## 6. Conclusions

This study presents a simple model for predicting flow behaviour and fibre formation during high moisture extrusion (HME) by incorporating the coupled effects of flow, temperature, phase separation, fibre alignment and wall-slip. The results demonstrate that cooling temperature plays a critical role in shaping the velocity profile, phase separation/syneresis and fibre alignment within the extruder die. Specifically, the model indicates a balance between cooling temperature and plug flow development to form oriented fibres near the die walls and randomly oriented fibres in the core while maintaining feasible flow conditions.

The model's mean-field approach to wall-slip and phase separation offers a practical compromise between physical accuracy and computational tractability. Validation through microscopy confirms the model's ability to qualitatively reproduce the spatial distribution of fibre orientations observed in the extrudate samples. However, model limitations remain, particularly in explaining any fibre alignment in the die centre solely through shear history.

Future work should aim to refine the model by incorporating additional mechanisms, such as extensional flow and barrel pre-orientation, and by quantifying fluid resistance to alignment through e.g. dead stop experiments. These enhancements will likely improve the model's predictive capability and support the development of more robust control strategies for fibre formation in HME processing.

## CRediT authorship contribution statement

**Erik Kaunisto:** Writing – review & editing, Writing – original draft, Validation, Methodology, Formal analysis, Conceptualization. **Camilla Öhgren:** Visualization, Validation, Methodology, Investigation, Data curation. **Niklas Lorén:** Writing – review & editing, Conceptualization. **Mats Stading:** Writing – review & editing, Writing – original draft, Project administration, Funding acquisition.

## Funding

The Swedish Scientific Board Formas is gratefully acknowledged for funding of the present study.

## Declaration of competing interest

The authors at RISE Research Institutes of Sweden (RISE) have no individual financial or personal gains from conducting and publishing the present original research.

## Acknowledgements

Leyla Dahl and Annika Krona at RISE – Department of Food Science and Innovation are gratefully acknowledged for their work with extrusion, obtaining extrudates and performing CLSM microscopy. Roland Kádár at Chalmers University of Technology is also gratefully acknowledged for fruitful discussions on fibre formation in meat analogues.

## Data availability

The data that has been used is confidential.

## References


Ardakani, H.A., Mitsoulis, E., Hatzikiriakos, S.G., 2013. Polytetrafluoroethylene paste extrusion: a fibrillation model and its relation to mechanical properties. Int. Polym. Process. 28 (3), 306–313. https://doi.org/10.3139/217.2744.

Cahn, J.W., Hilliard, J.E., 1958. Free energy of a Nonuniform system. I. Interfacial free energy. J. Chem. Phys. 28 (2), 258–267. https://doi.org/10.1063/1.1744102.

Chen, F.L., Wei, Y.M., Zhang, B., 2011. Chemical cross-linking and molecular aggregation of soybean protein during extrusion cooking at low and high moisture content. LWT - Food Sci. Technol. (Lebensmittel-Wissenschaft -Technol.) 44 (4), 957–962. https://doi.org/10.1016/j.lwt.2010.12.008.

Comsol, A., 2021. COMSOL Multiphysics Reference Manual, Version 6.0".

Cornet, S.H.V., Snel, S.J.E., Schreuders, F.K.G., van der Sman, R.G.M., Beyrer, M., van der Goot, A.J., 2022. Thermo-mechanical processing of plant proteins using shear cell and high-moisture extrusion cooking. Crit. Rev. Food Sci. Nutr. 62 (12), 3264–3280. https://doi.org/10.1080/10408398.2020.1864618.

Dekkers, B.L., Hamoen, R., Boom, R.M., Van Der Goot, A.J., 2018. Understanding fiber formation in a concentrated soy protein isolate - Pectin blend. J. Food Eng. 222, 84–92. https://doi.org/10.1016/j.jfoodeng.2017.11.014.

Di, Y., Ding, L., Gao, L., Huang, H., 2023. Association of meat consumption with the risk of gastrointestinal cancers: a systematic review and meta-analysis. BMC Cancer 23 (1), 782. https://doi.org/10.1186/s12885-023-11218-1.

Folgar, F., Tucker, C.L., 1984. Orientation behavior of Fibers in concentrated Suspensions. J. Reinforc. Plast. Compos. 3 (2), 98–119. https://doi.org/10.1177/073168448400300201.

Gerber, P.J.S., Henderson, H., Mottet, B., A, Opio, C., Dijkman, J.F., Tempio, G.A., 2013. Tackling Climate Change through Livestock – A Global Assessment of Emissions and Mitigation Opportunities. Food and Agriculture Organization of the United Nations (FAO), Rome.

Glenn, A.J., Wang, F., Tessier, A.J., Manson, J.E., Rimm, E.B., Mukamal, K.J., Sun, Q., Willett, W.C., Rexrode, K.M., Jenkins, D.J., Hu, F.B., 2024. Dietary plant-to-animal protein ratio and risk of cardiovascular disease in 3 prospective cohorts. Am. J. Clin. Nutr. 120 (6), 1373–1386. https://doi.org/10.1016/j.ajcnut.2024.09.006.

Grabowska, K.J., Tekidou, S., Boom, R.M., van der Goot, A.-J., 2014. Shear structuring as a new method to make anisotropic structures from soy–gluten blends. Food Res. Int. 64, 743–751. https://doi.org/10.1016/j.foodres.2014.08.010.

Guan, T., Sägesser, C., Villiger, R., Zychowski, L., Kohlbrecher, J., Dumpler, J., Mathys, A., Rühs, P., Fischer, P., Matsarskaia, O., 2024. In situ studies of plant-based meat analog texturization. Food Hydrocoll. 155, 110215. https://doi.org/10.1016/j.foodhyd.2024.110215.

Högg, E., Horneber, T., Rauh, C., 2017. Experimental and numerical analyses of the texturisation process of a viscoelastic protein matrix in a cooling die after high moisture extrusion cooking. Experimentelle Strömungsmechanik 25.

Högg, E., Horneber, T., Rauh, C., 2025. Modeling and experimental analysis of protein matrix solidification in cooling dies during high-moisture extrusion. Front. Food Sci. Technol. 5–2025. https://doi.org/10.3389/frfst.2025.1443376.

Kaunisto, E., Tsegaye, B., Kotzé, R., Wiklund, J., Kádár, R., Stading, M., 2025. Towards in-line rheology measurement of protein melts during high moisture extrusion by pulsed ultrasound velocimetry. J. Food Eng. 391. https://doi.org/10.1016/j.jfoodeng.2024.112461 (in press).

Kaunisto, E., Wassén, S., Stading, M., 2024. A thermodynamical finite element model of the fibre formation process during extrusion of high-moisture meat analogues. J. Food Eng. 362, 111760. https://doi.org/10.1016/j.jfoodeng.2023.111760.

Lorén, N., Altskär, A., Krona, A., Nilsson Pingel, T., Hall, S., Stading, M., Öhgren, C., 2025. Combined techniques to Understand the multiscale structure and Functionality of foods. In: Gillies, G., Rousseau, D. (Eds.), Soft Matter in Foods. Royal Society of Chemistry, pp. 210–233. https://doi.org/10.1039/9781837676699.

Nieuwland, M., Heijnis, W., van der Goot, A.-J., Hamoen, R., 2023. XRT for visualizing microstructure of extruded meat replacers. Curr. Res. Food Sci. 6, 100457. https://doi.org/10.1016/j.crfs.2023.100457.

Osen, R., Schweiggert-Weisz, U., 2016. High-moisture Extrusion: Meat Analogues.

Patil, P.D., Feng, J.J., Hatzikiriakos, S.G., 2006. Constitutive modeling and flow simulation of polytetrafluoroethylene (PTFE) paste extrusion. J. Non-Newtonian Fluid Mech. 139 (1), 44–53. https://doi.org/10.1016/j.jnnfm.2006.05.013.

Sandoval Murillo, J.L., Osen, R., Hiermaier, S., Ganzenmüller, G., 2019. Towards understanding the mechanism of fibrous texture formation during high-moisture extrusion of meat substitutes. J. Food Eng. 242, 8–20. https://doi.org/10.1016/j.jfoodeng.2018.08.009.

Slattery, J.C., 1999. Advanced Transport Phenomena. Cambridge University Press, Cambridge.

Steinfeld, H., 2006. Livestock's Long Shadow - Environmental Issues and Options, FAO. Food and Agriculture Organization of the United Nations (FAO), Rome.

Sägesser, C., Mair, T., Braun, A., Dumpler, J., Fischer, P., Mathys, A., 2025. Application of a shear cell for the simulation of extrusion to test the structurability of raw materials. Food Hydrocoll. 160, 110736. https://doi.org/10.1016/j.foodhyd.2024.110736.

Tammi, R., Kaartinen, N.E., Harald, K., Maukonen, M., Tapanainen, H., Smith-Warner, S. A., Albanes, D., Eriksson, J.G., Jousilahti, P., Koskinen, S., Laaksonen, M.A., Heikkinen, S., Pitkäniemi, J., Pajari, A.-M., Männistö, S., 2024. Partial substitution of red meat or processed meat with plant-based foods and the risk of colorectal cancer. Eur. J. Epidemiol. 39 (4), 419–428. https://doi.org/10.1007/s10654-024-01096-7.

van der Sman, R.G.M., van der Goot, A.J., 2023. Hypotheses concerning structuring of extruded meat analogs. Curr. Res. Food Sci. 6, 100510. https://doi.org/10.1016/j.crfs.2023.100510.

Vavlekas, D., Melo, L., Ansari, M., Grant, E., Fremy, F., McCoy, J.L., Hatzikiriakos, S.G., 2017. Role of PTFE paste fibrillation on Poisson's ratio. Polym. Test. 61, 65–73. https://doi.org/10.1016/j.polymertesting.2017.05.004.

Wittek, P., Ellwanger, F., Karbstein, H.P., Emin, M.A., 2021. Morphology development and flow characteristics during high moisture extrusion of a plant-based meat analogue. Foods 10 (8), 1753.

Zhang, X., Zhao, Y., Zhang, T., Zhang, Y., Jiang, L., Sui, X., 2022. High moisture extrusion of soy protein and wheat gluten blend: an underlying mechanism for the formation of fibrous structures. LWT 163, 113561. https://doi.org/10.1016/j.lwt.2022.113561.